24 May 2021

Sensitivity-Enhanced Microwave-Photonic Optical Fiber Interferometry based on the Vernier Effect

Chen Zhu

Jie Huang
Missouri University of Science and Technology, jieh@mst.edu

Sensitivity-enhanced microwave-photonic optical fiber interferometry based on the Vernier effect

CHEN ZHU[1,2] (iD) AND JIE HUANG[1,3] (iD)

[1]*Department of Electrical and Computer Engineering, Missouri University of Science and Technology, Rolla, MO 65409, USA*
[2]*cznwq@mst.edu*
[3]*jieh@mst.edu*

Abstract: This paper proposes optical carrier microwave interferometry (OCMI)-based optical fiber interferometers for sensing applications with improved measurement sensitivity with the assistance of the Vernier effect. Fabry-Perot interferometers (FPIs) are employed in the proof of concept. A single-FPI-OCMI system is first demonstrated for measurements of variations of temperatures by tracking the spectral shift of the interferogram in microwave domain. By cascading two FPIs with slightly different optical lengths, the Vernier effect is generated in the magnitude spectrum of the system with a typical amplitude-modulated signal. By tracking the shift of the envelope signal, temperature measurements are experimentally demonstrated with greatly enhanced sensitivity. The amplification factor for the measurement sensitivity can be easily adjusted by varying the length ratio of the two cascaded FPIs. In addition to the experimental demonstration, a complete mathematical model of the FPI-OCMI system and the mechanism for the amplified sensitivity due to Vernier effect is presented. Numerical calculations are also performed to verify the analytical derivations.

1. Introduction

Microwave photonics has been extensively explored in the past three decades for various applications such as photonic generation of high-quality microwave signals, high-speed processing of microwave signals, optically controlled phase array antennas, and high-speed photonic analog-to-digital conversion [1–3]. Intrigued by the research advancements in microwave photonics, an interesting concept called optical carrier-based microwave interferometry (OCMI) was proposed and experimentally demonstrated [4–6]. The essence of the OCMI concept is to interrogate optical interferometers (e.g., optical fiber interferometers) in microwave domain. The OCMI technique integrates the strengths from two disparate arenas, optics and microwaves, and has been employed to address the well-known issues faced by traditional optical fiber interferometers (OFIs). Optical fiber-based OCMI techniques were demonstrated to provide unique features that are particularly advantageous when it comes to sensing applications [6–8]. These attractive features include relieved requirements of accuracy during sensor fabrication, low dependence on multimode interference, insensitivity to variations in polarization of the probing light, and high-quality sensing signal (e.g., high signal-to-noise ratio and fringe visibility). Another prominent feature of the OCMI technique is the capability for fully distributed sensing with a satisfactory spatial resolution of a few centimeters [9,10]. This is because the phase of a microwave signal can be easily and accurately measured with a vector network analyzer (VNA). The phase spectrum of an OCMI system contains the spatial position information of external perturbations such as changes in temperature or strain. Both the magnitude and spatial position of the external perturbation can be determined from the complex reflection coefficient of the system. Thus, distributed and quantitative sensing is made possible using the OCMI technique [9].

Several mechanisms have been demonstrated as effective methods to enhance the measurement sensitivity of OFIs such as phase-shifted amplification technique [11,12] and Vernier effect [13]. Among them, Vernier effect is one of the simplest and most efficient approaches. In general, two cascaded OFIs with slightly different optical path differences (OPDs) are required to generate Vernier effect. The superposition of the two spectra of the two cascaded OFIs generates an amplitude-modulated (AM) spectrum as the output of the whole system. The free spectral range (FSR) of the resultant AM envelope is significantly greater than that of the two single OFIs. It is proven that the AM envelope is much more sensitive than the individual spectrum of the two OFIs. In other words, due to Vernier effect, the shift of the AM envelope in the output spectrum of two cascaded OFIs is more distinct compared to the spectral shift of a single OFI when subjected to the same external perturbation. So far, Vernier effect has been implemented in various types of OFIs such as Fabry-Perot interferometers (FPIs) [14,15], Sagnac interferometers [16], micro-ring resonators [17,18], and Mach-Zehnder interferometers (MZIs) [19,20]. These configurations were used for sensing different physical, chemical, and biological parameters with substantially improved sensitivity.

Very recently, we demonstrated a phase-shift-amplified optical fiber interferometer based on microwave photonics, where a destructive interference-based phase amplification technique was implemented in an OCMI-MZI system [21]. The phase sensitivity of the system to variations of OPD of the MZI was substantially improved due to the phase shift amplification technique. The magnification factor for phase sensitivity can be finely tuned by adjusting the transmission ratio of the two optical fiber arms of the MZI. In this paper, for the first time, we report the implementation of Vernier effect in an OCMI system for sensing applications with significantly improved measurement sensitivity. Optical fiber FPIs in an OCMI system are used for demonstration because FPIs work in a convenient reflection mode. We present a complete mathematical model for the sensitivity enhancement mechanism in the FPI-OCMI system due to Vernier effect. First, the capability of a single-FPI-OCMI system for the measurement of temperature variations is experimentally demonstrated. Enhancement of measurement sensitivity by cascading two FPIs in the OCMI system, with the assistance of the Vernier effect is then demonstrated. The amplification factor can also be tuned by simply adjusting the length ratio of two cascaded FPIs. The results from the experimental investigations match well with the theoretical expectations.

2. Principle and numerical investigation

2.1. Single-FPI-OCMI system

Figure 1 shows the schematic of a single-FPI-OCMI system, where a single FPI is connected to an OCMI system. A vector network analyzer (VNA, Agilent 8753ES) and a direct modulation laser (HP 83402B, 1300 nm, 300 kHz-6 GHz) are employed as the microwave source and the source of the optical carrier in the system, respectively. The output from Port 1 of the VNA is first amplified using an RF amplifier before being injected into the RF input of the laser. The intensity-modulated light output from the laser, where the optical signal is the carrier and the microwave signal is the envelope, is launched into the optical fiber FPI via a fiber-optic circulator. The reflected signal from the FPI sensor is redirected to a high-speed photodetector (HP 11982A). After optoelectronic conversion, the RF output from the photodetector is sent to Port 2 of the VNA. By sweeping the frequency of the microwave signal, the reflection spectrum (i.e., S_{21} from the VNA, including phase and magnitude spectra) of the FPI sensor in the microwave domain is obtained. Applying an inverse Fourier transform to the recorded S_{21}, the time-domain signal of the FPI-OCMI system is calculated, where the spatial positions and effective reflectivity of the two reflectors of the FPI sensor can be unambiguously determined.

A mathematical model of the single-FPI-OCMI system is first developed. The intensity-modulated probing light is injected into the FPI sensor and gets reflected. Neglecting the transmission loss of the first reflector, the electric field E_{total} of the reflected optical signal is
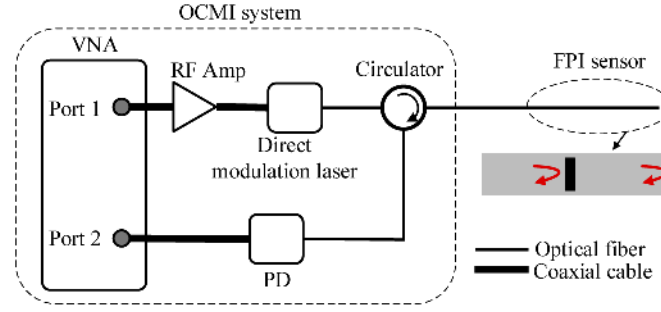
Fig. 1. Schematic of a single-FPI-OCMI system; vector network analyzer (VNA), RF amplifier (RF Amp), photodetector (PD). The FPI consists of two reflectors, where the first reflector is fabricated by creating an air gap between the lead-in optical fiber and the lead-out optical fiber supported in fiber ferrules. The lead-in fiber and lead-out fiber are aligned face-to-face with an air gap, with the assistance of a ferrule mating sleeve. Note that the effective reflection of the air-gap configuration can be adjusted by varying the gap distance [22]. The second reflector is the cleaved end facet of the optical fiber.

given by

$$E_{total} = E_1 + E_2 \tag{1}$$

where E_1 and E_2 represent the electric field of the intensity-modulated optical signal reflected by the two reflectors of the FPI sensor and are given by

$$E_i = m_i(t)E_{o,i} = \sqrt{1 + M\cos\left[2\pi f(t + \frac{W}{c} + \frac{2nz_i}{c})\right]} \cdot \Gamma_i A \exp\left\{-j\left[\omega\left(t + \frac{2nz_i}{c}\right)\right]\right\}, \ i = 1, 2 \tag{2}$$

where M and f are the amplitude and frequency of the microwave modulation signal, respectively; W represents the common electrical and optical length in the system; c is the speed of light in vacuum; n represents the refractive index of the core of the optical fiber; z_i denotes the spatial location of the i-th reflector; t is the time term; A and ω are the amplitude and angular frequency of the electric field of the probing light; Γ_i denotes reflection coefficient of the i-th reflector. Assume that the spectral width of the laser source is ω_{max}-ω_{min}, the total power of the reflected optical signal is thus given by

$$|E_{total}|^2 = \int_{\omega_{min}}^{\omega_{max}} (|E_1|^2 + |E_2|^2)d\omega = \Gamma_1{}^2A^2 + \Gamma_2{}^2A^2 + \Gamma_1{}^2A^2M\cos\left[2\pi f(t + \frac{W}{c} + \frac{2nz_1}{c})\right]$$
$$+ \Gamma_2{}^2A^2M\cos\left[2\pi f(t + \frac{W}{c} + \frac{2nz_2}{c})\right] \tag{3}$$

Note that the cross-product components are neglected. This is because in a typical FPI-OCMI system, the length of the FPI sensor (i.e., the distance between the two reflectors, z_1-z_2) is sufficiently greater than the coherence length of the laser source, leading to the cross-product components approaching zero. The total power of the optical signal includes a DC term and the superposition of two microwave signals with a frequency of f. The OCMI system uses synchronized detection to eliminate the DC term in Eq. (3), and the magnitude and phase of the superimposed microwave signal at frequency f are recorded (i.e., S_{21}). Thus, the signal S_{21}

measured by the VNA is given by

$$S = S_o \cos(2\pi f t + \Phi) \tag{4}$$

where S_o and Φ denote the magnitude and phase of the output microwave signal, respectively, and can be expressed as

$$
\begin{aligned}
S_o &= g\sqrt{\Gamma_1{}^4 A^4 M^2 + \Gamma_2{}^4 A^4 M^2 + 2\Gamma_1{}^2\Gamma_2{}^2 A^4 M^2 \cos(2\pi f \tfrac{2nz_1 - 2nz_2}{c})} \\
\Phi &= \frac{\Gamma_1{}^2 \sin\left[2\pi f\left(\frac{W}{c} + \frac{2nz_1}{c}\right)\right] + \Gamma_2{}^2 \sin\left[2\pi f\left(\frac{W}{c} + \frac{2nz_2}{c}\right)\right]}{\Gamma_1{}^2 \cos\left[2\pi f\left(\frac{W}{c} + \frac{2nz_1}{c}\right)\right] + \Gamma_2{}^2 \cos\left[2\pi f\left(\frac{W}{c} + \frac{2nz_2}{c}\right)\right]}
\end{aligned}
\tag{5}
$$

where g represents the gain of the photodetector. The first term in Eq. (5) indicates that the magnitude of the output microwave signal varies as a sinusoidal function of the microwave frequency and the OPD of the FPI sensor (i.e., $2nz_1 - 2nz_2$) in the OCMI system, which is the same as a typical optical-domain FPI. By sweeping the frequency, the microwave interferogram of the FPI-OCMI system can be obtained; by tracking the shift of the microwave interferogram, the change in OPD of the FPI sensor can be determined. Therefore, the FPI-OCMI system can be used as a sensing device for measuring parameters that can be correlated to the OPD of the FPI, e.g., variations of temperature or strain. It should be noted that the phase term in Eq. (5) is a function of the summation of the electric and optical lengths in the system. In other words, the spatial locations of the two reflectors of the FPI can also be determined by applying the inverse Fourier transform to Eq. (5). Thus, multiplexing a series of FPIs in the OCMI system for distributed sensing is made possible [9].

2.2. Numerical investigation of a single FPI for temperature sensing

As mentioned above, the FPI-OCMI system can be used for sensing by tracking the shift of the microwave interferogram. Let's further examine the magnitude term in Eq. (5). For simplicity, we assume that the reflectivities of the two reflectors in the FPI sensor are the same, i.e., $\Gamma_1 = \Gamma_2 = \Gamma$, then the magnitude term can be simplified as

$$S_o = 2g\Gamma^2 A^2 M \left| \cos(2\pi f \frac{nL_0}{c}) \right| \tag{6}$$

where $L_0 = z_2 - z_1$, denoting the physical distance between the two reflectors of the FPI sensor, i.e., the length of the FPI. According to the phase-matching condition, the resonance frequencies f_{res} and the FSR of the magnitude spectrum of the FPI-OCMI system is given by

$$
\begin{aligned}
f_{res} &= \frac{2k+1}{4}\frac{c}{nL_0} \\
FSR &= \frac{c}{2nL_0}
\end{aligned}
\tag{7}
$$

According to Eq. (7), the temperature sensitivity of the single-FPI-OCMI system K_0 can be derived as

$$K_0 = \frac{\Delta f_{res}}{\Delta T} \approx -f_{res}(\xi + \alpha) \tag{8}$$

where Δf_{res} and ΔT represent the change in resonance frequency and the change in temperature of the FPI sensor, respectively; ξ and α denote thermo-optic coefficient and thermal expansion coefficient of the optical fiber in the FPI. The temperature sensitivity is also a function of the resonance frequency of the system, and the higher the resonance frequency, the larger the sensitivity.

Figure 2 presents the numerical investigations of the single-FPI-OCMI system based on Eq. (6). In the calculation, the length of the FPI was set to 0.5 m. Figure 2(a) shows the calculated

magnitude spectrum in the frequency range of 0–2 GHz. Discrete resonance frequencies can be observed, and the FSR was determined to be 204.3 MHz, which matched well with Eq. (7). The shift in resonance frequencies as a function of variations of temperature is plotted in Fig. 2(b). Three different resonance frequencies were monitored in the investigation; the higher the resonance frequency, the larger the temperature sensitivity. The numerically calculated sensitivity matched well with the analytical results (see Eq. (8)).
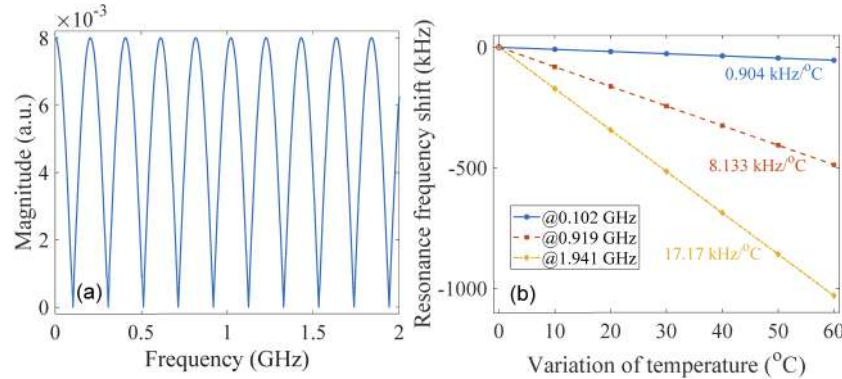

Fig. 2. Numerical investigations of the single-FPI-OCMI system. (a) Calculated magnitude spectrum of the single-FPI-OCMI system. The length of the FPI was set to 0.5 m. (b) Shift in resonance frequencies of the single-FPI-OCMI system as a function of variations of temperature. Three different resonance frequencies were monitored. The parameters used in the calculation were: Γ=0.1; A=1; M=0.8; g=0.5; ξ=8.3×10^{-6}/°C; α=5.5×10^{-7}/°C; n=1.468; L_0=0.5 m; W=0.2 m.

2.3. Numerical investigation of two cascaded FPIs for temperature sensing based on the Vernier effect

Figure 3 shows a schematic diagram of two cascaded FPIs connected to an OCMI system, which is constructed to demonstrate the Vernier effect-induced sensitivity enhancement. The first interferometer, i.e., FPI$_{ref}$, is employed as a reference interferometer, while the second interferometer, FPI$_{sen}$, is used for sensing. To generate Vernier effect, the OPD of the two FPIs is set to be slightly different.
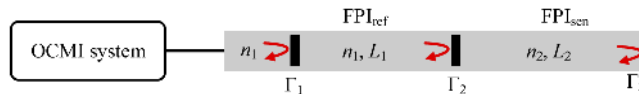

Fig. 3. A schematic diagram of two cascaded FPIs connected to an OCMI system. The first two reflectors are created by introducing an air gap between the lead-in fiber and lead-out fiber. The third reflector is the cleaved facet of the optical fiber at the end. The reflectivities of the three reflectors are Γ_1, Γ_2, and Γ_3. The first FPI is used as a reference interferometer, while the second FPI is used for sensing. n_1 represents the refractive index of the core of the lead-in optical fiber and the fiber in FPI$_{ref}$; n_2 denotes the refractive index of the core of the optical fiber in FPI$_{sen}$. L_1 and L_2 represent the length of FPI$_{ref}$ and FPI$_{sen}$, respectively.

Derivation of the analytical model for the two-cascaded-FPIs-OCMI system follows the same procedure shown in section *2.1*. The magnitude spectrum of the system can be expressed as

$$S_o = g \sqrt{ \begin{array}{l} \Gamma_1{}^4 A^4 M^2 + \Gamma_2{}^4 A^4 M^2 + \Gamma_3{}^4 A^4 M^2 + \\ 2\Gamma_1{}^2\Gamma_2{}^2 A^4 M^2 \cos(\phi_{12}) + 2\Gamma_2{}^2\Gamma_3{}^2 A^4 M^2 \cos(\phi_{23}) + 2\Gamma_1{}^2\Gamma_3{}^2 A^4 M^2 \cos(\phi_{13}) \end{array} } \tag{9}$$

where

$$\phi_{12} = 2\pi f \frac{2n_1 L_1}{c}, \quad \phi_{23} = 2\pi f \frac{2n_2 L_2}{c}, \quad \phi_{13} = 2\pi f \frac{2n_1 L_1 + 2n_2 L_2}{c} \tag{10}$$

Figure 4 shows the calculated magnitude spectra of the two individual FPIs (i.e., FPI$_{ref}$ and FPI$_{sen}$) and the cascaded FPIs according to Eqs. (6), (9), and (10). Sinusoidal signals for both the reference FPI and the sensing FPI were obtained, as expected. An amplitude-modulated signal was obtained for the two cascaded FPIs due to the beating between the two individual spectra. Two envelopes are indicated in the figure. The analytical expression for envelope 1 can be derived from Eq. (9) as

$$S_1 = \left| A_{en1} \cos(2\pi f \frac{n_2 L_2 - n_1 L_1}{c}) \right| + D_1 \tag{11}$$

where A_{en1} and D_1 denote amplitude and offset of the signal; Similarly, the analytical expression for envelope 2 can be expressed as

$$S_2 = A_{en2} \cos(2\pi f \frac{n_2 L_2 - n_1 L_1}{c}) + D_2 \tag{12}$$

where A_{en2} and D_2 denote the amplitude and offset of envelope 2. By tracking the spectral shift of the envelopes, both envelopes can be used for sensing applications with improved sensitivity. Here, we focus on investigating envelope 2. According to the phase-matching condition, the dip frequencies and the FSR of the envelope signal are given by

$$\begin{aligned} f_{dip} &= \frac{2k+1}{2} \left| \frac{c}{n_1 L_1 - n_2 L_2} \right| \\ FSR_{en} &= \frac{c}{|n_1 L_1 - n_2 L_2|} \end{aligned} \tag{13}$$

Correlating the FSR of envelope 2 with the FSR of the two individual FPIs gives

$$FSR_{en} = 2 \frac{FSR_{ref} FSR_{sen}}{|FSR_{ref} - FSR_{sen}|} \tag{14}$$

where FSR_{ref} and FSR_{sen} are the FSR of the reference FPI and the sensing FPI, respectively. Equation (14) matched well with the optical-domain cascaded FPIs [14].

According to Eq. (13), the shift of the dip frequency Δf_{dip} of the envelope signal due to a temperature variation of ΔT in the sensing FPI can be expressed as

$$\Delta f_{dip} = \frac{2k+1}{2} \left\{ \frac{c}{|n_1 L_1 - [n_2 L_2 + n_2 L_2(\xi \Delta T + \alpha \Delta T)]|} - \frac{c}{|n_1 L_1 - n_2 L_2|} \right\} \tag{15}$$

Further deriving Eq. (15), the temperature sensitivity of the two-cascaded-FPIs-OCMI is obtained as

$$K_1 = \frac{\Delta f_{dip}}{\Delta T} \approx f_{dip}(\xi + \alpha) \frac{n_2 L_2}{n_1 L_1 - n_2 L_2} \tag{16}$$

Comparing Eq. (8) and Eq. (16), the amplification factor V for temperature sensitivity due to Vernier effect can be obtained

$$V = \frac{K_1}{K_0} = \frac{n_2 L_2}{n_2 L_2 - n_1 L_1} \tag{17}$$
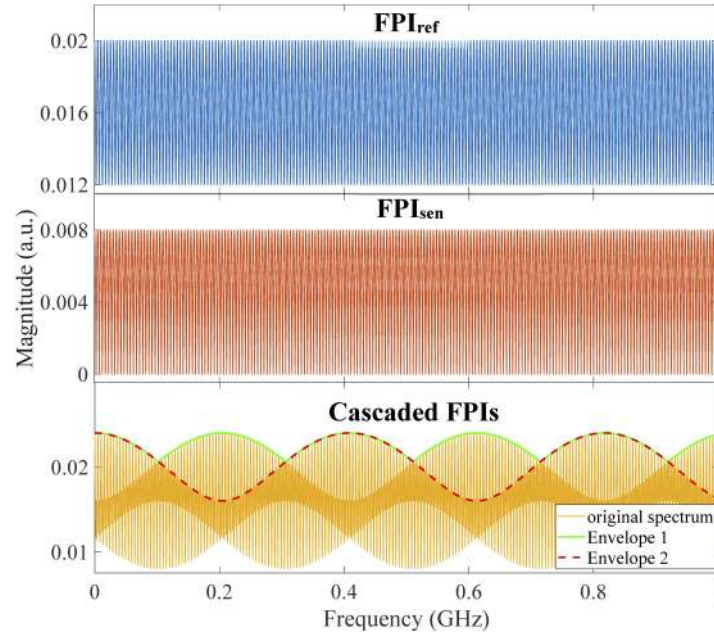
Fig. 4. Calculated magnitude spectra of the reference FPI (top), sensing FPI (middle), and the two cascaded FPIs (bottom). The parameters used in the calculation were: Γ_1=0.2; Γ_2=0.1; Γ_3=0.1; A=1; M=0.8; g=0.5; n_1=n_2=1.468; W=0.2 m; L_1=20 m; L_2=20.5 m.

In the study herein, the two FPIs were constructed using the same single-mode fibers, i.e., n_1=n_2, and thereby Eq. (17) can be simplified as

$$V = \frac{1}{1 - L_1/L_2} \tag{18}$$

Equation (18) indicates that a positive amplification factor is obtained as $L_2 > L_1$; a negative amplification factor is expected as $L_2 < L_1$; and, as the length ratio of the two FPIs approaches unity, the larger the amplification factor is.

Numerical calculations based on Eq. (9) were performed to verify the analytical model of the sensitivity amplification mechanism in the two-cascaded-FPIs-OCMI system. Figure 5 presents the results. Note that envelope 2 (see Fig. 4) of the calculated spectrum for the cascaded FPIs was first obtained using a curve fit method. Measurements of temperature variations of the sensing FPI were performed by tracking the shift of the envelope signal. Figure 5(a) shows the calculated envelope signals of the two-cascaded-FPIs-OCMI system for different temperature settings of the sensing FPI. In this case, L_2=100.5 m and L_1=100 m, i.e., $L_2 > L_1$. As the temperature increased, the envelope signal shifted to the lower frequency region. The shift in the dip frequencies of the envelope signal as a function of temperature variations is plotted in Fig. 5(b). Three different dip frequencies were monitored, and as shown in the figure, the higher the dip frequency, the larger the sensitivity. Figure 5(c) shows the calculated envelope signals where L_2=99.5 m, and L_1=100 m, i.e., $L_2 < L_1$, for different temperature settings of the sensing FPI. The envelope signal shifted to the higher frequency region as temperature increased. Figure 5(d) shows the shift in dip frequencies as a function of temperature variations. Similarly, three dip frequencies were monitored in the calculation, and the higher the dip frequency, the larger the sensitivity. The obtained temperature sensitivities in Fig. 5(b) and (d) matched well with the analytical results according to Eq. (16). For the first case where $L_2 > L_1$, a positive amplification factor of approximately 182 was obtained, which was close to the amplification factor 201 obtained from

Eq. (18). For the second case where $L_2 < L_1$, a negative amplification factor of approximately -223 was obtained, approaching the amplification factor -199 from the analytical expression.
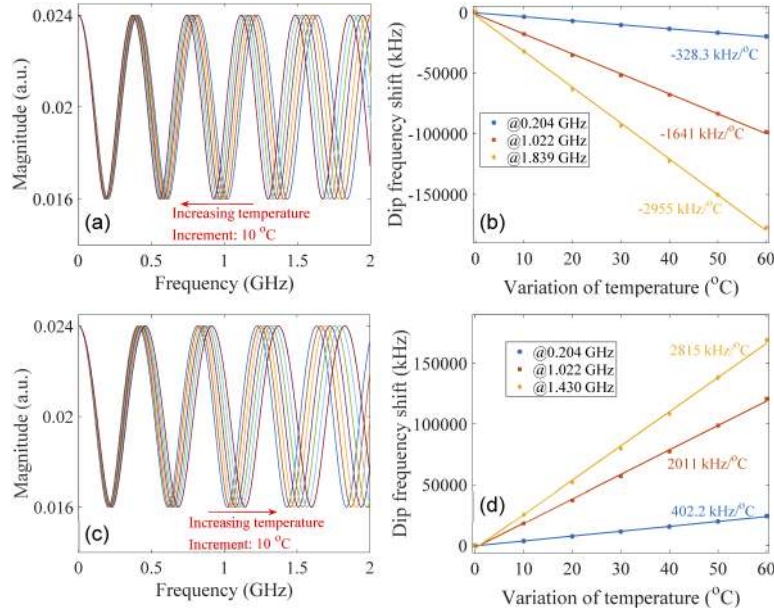

Fig. 5. Numerical investigations of the two-cascaded-FPIs-OCMI system for temperature sensing. (a) The evolution of the envelope signal as temperature increased in steps of 10 °C when $L_2 > L_1$. (b) Shift in dip frequencies as a function of variations of temperature. In (a) and (b), $L_2 = 100.5$ m and $L_1 = 100$ m. (c) The evolution of the envelope signal as temperature increased in steps of 10 °C when $L_2 < L_1$. (d) Shift in dip frequencies as a function of variations of temperature. In (c) and (d), $L_2 = 99.5$ m and $L_1 = 100$ m. Other parameters used in the calculation were: $\Gamma_1 = 0.2$; $\Gamma_2 = 0.1$; $\Gamma_3 = 0.1$; $A = 1$; $M = 0.8$; $g = 0.5$; $n_1 = n_2 = 1.468$; $W = 0.2$ m; $\xi = 8.3 \times 10^{-6}/°C$; $\alpha = 5.5 \times 10^{-7}/°C$.

3. Experimental results and discussion

3.1. Demonstration of the single FPI-OCMI system for temperature sensing

A single-FPI-OCMI system was first constructed as schematically shown in Fig. 1. Figure 6 shows the characterization results of the system. Note that the VNA used in the experiment has a built-in Fourier transform function. Therefore, the time-domain signal of the OCMI system, obtained by applying an inverse Fourier transform to the complex S_{21} signal, can be monitored in real-time. The time-domain signal reveals the spatial locations of the reflectors in the FPI. Figure 6(a) shows the time-domain signal of the single-FPI-OCMI system. Two peaks could be observed in the signal, which correspond to the two reflectors of the FPI. The strength of the peak indicates the effective reflectivity of the reflector. The time delay between the two reflectors, the round-trip delay of the interferometer, was determined to be 74.383 ns. Thus, the physical distance between the two reflectors was calculated to be 7.600 m given the refractive index of the fiber core to be 1.468. Figure 6(b) shows the measured magnitude spectrum, i.e., the interferogram in frequency domain, over a frequency range of 1–1.2 GHz. Discrete resonance frequencies could be observed, as expected. The FSR of the spectrum was found to be 13.444 MHz, which matched well with Eq. (7) provided that the length of the FPI is 7.600 m.

The temperature response of the single-FPI-OCMI system was subsequently tested. A section of the optical fiber with a length of approximately 4.52 m in the FPI was heated using a water
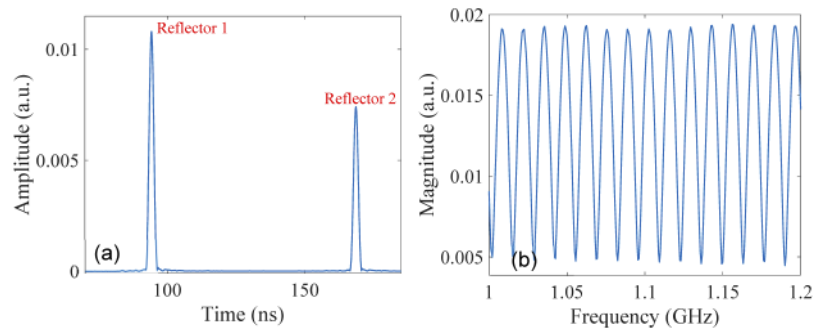
Fig. 6. Characterization results of the constructed single-FPI-OCMI system. (a) Time-domain signal of the single-FPI-OCMI system. (b) Measured microwave interferogram.

bath. Figure 7 presents the results of this test. Figure 7(a) shows the measured magnitude spectra over a frequency range of 1–1.02 GHz for different settings of temperature. The spectrum shifted to the lower frequency region as the applied temperature increased, as expected. The measured resonance frequency shift at ~1.002 GHz and ~2.010 GHz as a function of temperature is plotted in Fig. 7(b). Linear curve fits were applied to the data sets, with the slopes determined as −4.755 kHz/°C and −10.04 kHz/°C. A higher sensitivity was obtained for the larger resonance frequency at 2.010 GHz, which was expected from Eq. (8). Given the length of the fiber that was heated in the experiment to be ~4.52 m, the theoretical temperature sensitivities could be determined to be −5.274 kHz/°C and −10.58 kHz/°C. The measured sensitivities matched well with the theoretical values.
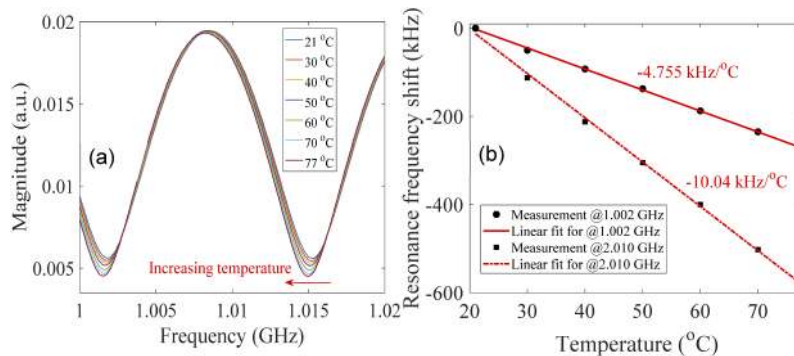

Fig. 7. Temperature sensing using the single-FPI-OCMI system. (a) Measured magnitude spectra of the system over a frequency range of 1–1.02 GHz for different settings of temperature. (b) Measured resonance frequency shift at ~1.002 GHz and ~2.010 GHz as a function of temperature, as depicted by black dots. Linear curve fits were applied to the measured data sets, as depicted by red lines.

3.2. Demonstration of the two-cascaded-FPIs-OCMI system for temperature sensing with enhanced sensitivity based on the Vernier effect

A two-cascaded-FPIs-OCMI system was constructed for demonstrating the sensitivity enhancement for temperature sensing based on Vernier effect. Figure 8 presents the characterization results of the system. Figure 8(a) shows the measured time-domain signal of the system. The three peaks correspond to the three reflectors of the two cascaded FPIs, as schematically illustrated in Fig. 3. The optical fiber section between reflector 1 and reflector 2 was employed as the reference

FPI, and the optical fiber section between reflector 2 and reflector 3 was used as the sensing FPI. The time delays between the two adjacent reflectors were found to be 74.063 ns and 83.726 ns. Thus, the lengths of the reference FPI and the sensing FPI were determined to be 7.568 m and 8.555 m, respectively. Figure 8(b) shows the measured magnitude spectrum of the system in a frequency range of 1–1.5 GHz. An amplitude-modulated signal was obtained, as expected. The envelope is also indicated in the figure. The FSR of the envelope was found to be 207.105 MHz, which matched well with the theoretical value of 207.051 MHz obtained from Eq. (13).
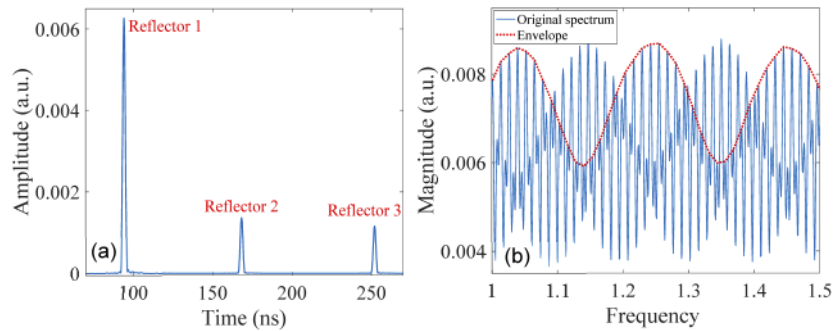

Fig. 8. Characterization result of the constructed two-cascaded-FPIs-OCMI system. (a) Time-domain signal of the system. (b) Measured magnitude spectrum of the system. The envelope is also indicated in the figure.

Temperature measurements were performed using the two-cascaded-FPIs-OCMI system. A section of the optical fiber with a length of approximately 6.48 m in the sensing FPI (with a total length of 8.555 m) was heated using a water bath, where the temperature was increased from 20 °C to 80 °C in steps of 10 °C. The reference FPI was kept at room temperature in the experiment. Figure 9 gives the measured responses of the system. Figure 9(a) shows the measured envelope signals at ~1.348 GHz (one of the dip frequencies, see Fig. 8(b)) for different settings of temperature. Curve fits using a four-degree polynomial model were applied to the measured datasets and the fitted models are plotted in the figure. The envelope shifted to the lower frequency region as temperature increased, which matched well with Fig. 5(a). Differentiating the curve-fitted models, the dip frequencies where the derivative reaches zero can be determined. The obtained dip frequency as a function of temperature is plotted in Fig. 9(b). The slope represents the temperature sensitivity and was determined to be −80.23 kHz/°C using a linear curve fit. The corresponding temperature sensitivity of the single-FPI-OCMI system (i.e., without sensitivity amplification) could be determined to be −9.036 kHz/°C according to Eq. (8). The measured sensitivity of the two-cascaded-FPIs-OCMI system reveals an amplification factor of 8.9. According to Eq. (16), the theoretical sensitivity can be calculated to be −78.32 kHz/°C, corresponding to an amplification factor of 8.7. The experiment demonstrates an improved sensitivity for the two-cascaded-FPIs-OCMI system based on Vernier effect for temperature measurements. The stability of the system after the sensitivity amplification needs to be further investigated.

An additional experiment was performed to demonstrate that the amplification factor based on Vernier effect could be tuned by adjusting the length ratio between the reference FPI and the sensing FPI in the two-cascaded-FPIs-OCMI system. In the investigation, the length of the sensing FPI was reduced to 7.854 m while the length of the reference FPI remained as 7.568 m. The same temperature experiment was performed, where a section of the optical fiber with a length of approximately 6.48 m in the sensing FPI (with a total length of 7.854 m) was heated using a water bath. Figure 10 presents the investigation results of the modified system. Figure 10(a) shows the measured magnitude spectrum of the system. Similar to Fig. 8(b), an
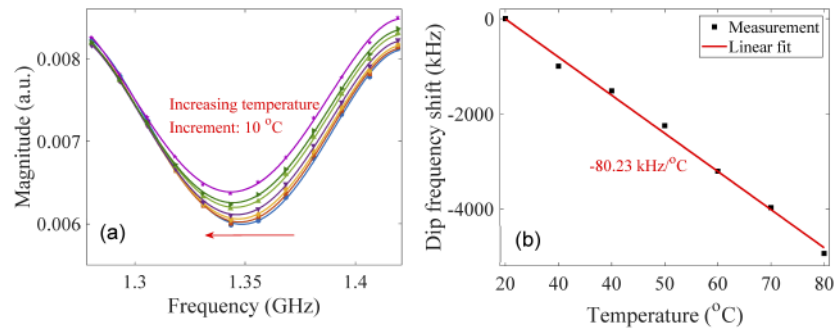
Fig. 9. Temperature sensing using the two-cascaded-FPIs-OCMI system. In the system, the lengths of the reference and sensing FPIs were 7.568 m and 8.555 m, respectively. (a) The envelope signals at ~1.348 GHz for different settings of temperature of the sensing FPI. The measured signals are depicted by discrete dots. Polynomial curve fits were applied to the measured data sets; the fitted models are depicted by solid lines. (b) Shift of the dip frequency at ~1.348 GHz as a function of temperature. Linear curve fit was applied to the measured data sets.

envelope emerged in the magnitude spectrum due to the cascaded configuration. The FSR of the envelope was found to be approximately 714.500 MHz. Figure 10(b) presents the dip frequencies of the envelope signals at ~1.436 GHz (obtained using the curve fit approach mentioned above) as a function of temperatures. A linear curve fit was applied to the measured discrete data sets, and the slope of the fitted curve was determined to be −266.1 kHz/°C, corresponding to an amplification factor of 25.4, which was close to the theoretical value (i.e., 27.5). The obtained sensitivity, i.e., −266.1 kHz/°C at ~1.436 GHz is approximately three times greater than the sensitivity obtained in the previous experiment, −80.23 kHz/°C at 1.348 GHz. This is expected because the length ratio of the reference FPI to the sensing FPI was increased from 0.8845 (7.568/8.555) to 0.9636 (7.568/7.854). The increase in the length ratio resulted in a substantial increase in the amplification factor, as can be expected from Eq. (18). Therefore, this experiment demonstrates that the amplification factor of the two-cascaded-FPIs-OCMI system can be flexibly tuned by adjusting the length ratio between the reference FPI and the sensing FPI in the system.
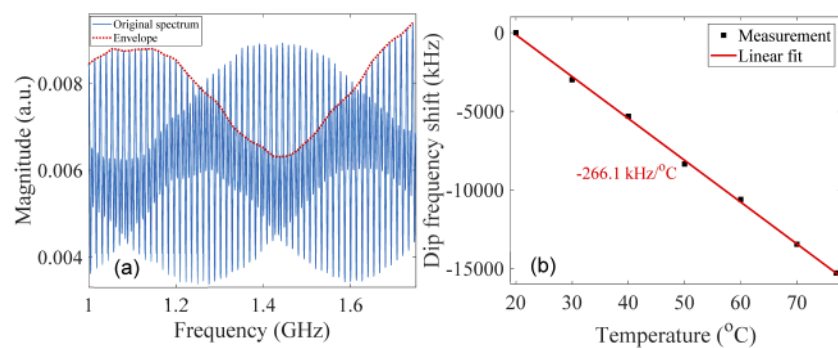

Fig. 10. Characterization result of the constructed two-cascaded-FPIs-OCMI system for temperature sensing where the lengths of the reference and sensing FPIs were 7.568 m and 7.854 m, respectively. (a) Measured magnitude spectrum of the system. The envelope is also plotted in a dashed-red line. (b) Shift of the dip frequency at ~1.436 GHz as a function of temperature. The dip frequencies were obtained using the polynomial curve fit approach as mentioned above. Linear curve fit was applied to the discrete data sets to determine the measurement sensitivity, as depicted by the red line.

It is worth mentioning that the fundamental limit of the amplification factor based on Vernier effect is the bandwidth of the microwave modulation signals. Sensing applications of the two-cascaded-FPIs-OCMI system are performed by tracking the shift of the envelope of the magnitude spectrum. According to Eqs. (13) and (18), the closer the length ratio of the two FPIs approaches unity, the larger the amplification factor and the larger the FSR of the envelope (i.e., the sensing signal). Given the limited frequency bandwidth of the microwave source (ΔB), the largest FSR that can be unambiguously and accurately determined from the magnitude spectrum is restricted to $\sim \Delta B$. Therefore, the largest amplification factor is given by

$$V_{\max} \approx \frac{nL_2 \Delta B}{c} \tag{19}$$

As can be seen, for a given frequency bandwidth, the larger the length of the sensing interferometer, the larger the amplification factor that can be theoretically achieved. Compared to the phase-shift-amplification-based system [21], the Vernier-effect-amplification-based system requires the acquisition of the magnitude spectrum to calculate the measurands, which limits the dynamic response of the sensor system. However, the Vernier-effect-based system is easier to implement, and the amplification factor can be flexibly adjusted by simply tuning the length ratio of the two cascaded FPIs. Compared to the fiber ring filter-based system [23], the FPI-based system reported in this study works in a more convenient reflection mode and is more compact since only one string of fiber is needed to generate Vernier effect for sensitivity amplification. Also, a complete analytical analysis is for the first time developed to mathematically verify that Vernier effect can be generated in cascaded microwave-photonic interferometers and can be utilized to amplify the measurement sensitivity. More importantly, the cascaded FPIs-based sensitivity amplification demonstrated here lays the groundwork for the development of a fully distributed optical fiber sensor based on OCMI with significantly improved sensitivity enabled by Vernier effect.

4. Conclusion

A method using Vernier effect for improving the sensitivity of optical fiber interferometers based on OCMI was proposed and experimentally demonstrated. We first presented a mathematical model for a single-FPI-OCMI system. By cascading two FPIs with slightly different optical lengths, Vernier effect was generated in the magnitude spectrum of the OCMI system. A complete mathematical model for the two-cascaded-FPIs-OCMI system and the mechanism of the Vernier effect-induced sensitivity enhancement was discussed. Numerical calculations were subsequently performed to verify the analytical derivations. Finally, temperature measurements were performed using a single-FPI-OCMI system and a two-cascaded-FPIs-OCMI system. The results verified substantially improved sensitivities due to Vernier effect in the two-cascaded-FPIs-OCMI system. The amplification for sensitivity could also be tuned by varying the length ratio of the cascaded FPIs, the closer the ratio approached unity, the larger the amplification factor. In addition to the FPIs demonstrated in this paper, Vernier effect-amplified optical fiber interferometry can also be implemented with other interferometers such as the Mach-Zehnder interferometer and the Michelson interferometer for measuring other quantities, such as strain and lateral force.

Disclosures. The authors declare no conflicts of interest.

Data availability. Data underlying the results presented in this paper are not publicly available at this time but may be obtained from the authors upon reasonable request.

References

1. J. Yao, "Microwave photonics," J. Lightwave Technol. **27**(3), 314–335 (2009).
2. J. Capmany and D. Novak, "Microwave photonics combines two worlds," Nat. Photonics **1**(6), 319–330 (2007).
3. J. Hervás, A. L. Ricchiuti, W. Li, N. H. Zhu, C. R. Fernández-Pousa, S. Sales, M. Li, and J. Capmany, "Microwave photonics for optical sensors," IEEE J. Sel. Top. Quantum Electron. **23**(2), 327–339 (2017).
4. J. Huang, X. Lan, H. Wang, L. Yuan, and H. Xiao, "Optical carrier-based microwave interferometers for sensing application," in *Fiber Optic Sensors and Applications XI*, (International Society for Optics and Photonics, 2014), 90980H.
5. T. Wei, J. Huang, X. Lan, Q. Han, and H. Xiao, "Optical fiber sensor based on a radio frequency Mach–Zehnder interferometer," Opt. Lett. **37**(4), 647–649 (2012).
6. J. Huang, "*Optical fiber based microwave-photonic interferometric sensors*," (Clemson University, 2015).
7. J. Huang, X. Lan, Y. Song, Y. Li, L. Hua, and H. Xiao, "Microwave interrogated sapphire fiber Michelson interferometer for high temperature sensing," IEEE Photonics Technol. Lett. **27**(13), 1398–1401 (2015).
8. L. Hua, Y. Song, J. Huang, X. Lan, Y. Li, and H. Xiao, "Microwave interrogated large core fused silica fiber Michelson interferometer for strain sensing," Appl. Opt. **54**(24), 7181–7187 (2015).
9. J. Huang, X. Lan, M. Luo, and H. Xiao, "Spatially continuous distributed fiber optic sensing using optical carrier based microwave interferometry," Opt. Express **22**(15), 18757–18769 (2014).
10. L. Hua, Y. Song, B. Cheng, W. Zhu, Q. Zhang, and H. Xiao, "Coherence-length-gated distributed optical fiber sensing based on microwave-photonic interferometry," Opt. Express **25**(25), 31362–31376 (2017).
11. M. B. Ayun, A. Schwarzbaum, S. Rosenberg, M. Pinchas, and S. Sternklar, "Photonic radio frequency phase-shift amplification by radio frequency interferometry," Opt. Lett. **40**(21), 4863–4866 (2015).
12. M. B. Ayun, S. Rosenberg, D. Gotliv, and S. Sternklar, "Fundamental Limits of Photonic RF Phase-Shift Amplification by RF Interferometry," J. Lightwave Technol. **35**(10), 1906–1913 (2017).
13. M. La Notte, B. Troia, T. Muciaccia, C. E. Campanella, F. De Leonardis, and V. Passaro, "Recent advances in gas and chemical detection by Vernier effect-based photonic sensors," Sensors **14**(3), 4831–4855 (2014).
14. M. Quan, J. Tian, and Y. Yao, "Ultra-high sensitivity Fabry–Perot interferometer gas refractive index fiber sensor based on photonic crystal fiber and Vernier effect," Opt. Lett. **40**(21), 4891–4894 (2015).
15. Y. Zhao, P. Wang, R. Lv, and X. Liu, "Highly sensitive airflow sensor based on Fabry–Perot interferometer and Vernier effect," J. Lightwave Technol. **34**(23), 5351–5356 (2016).
16. L.-Y. Shao, Y. Luo, Z. Zhang, X. Zou, B. Luo, W. Pan, and L. Yan, "Sensitivity-enhanced temperature sensor with cascaded fiber optic Sagnac interferometers based on Vernier-effect," Opt. Commun. **336**, 73–76 (2015).
17. L. Jin, M. Li, and J.-J. He, "Highly-sensitive silicon-on-insulator sensor based on two cascaded micro-ring resonators with vernier effect," Opt. Commun. **284**(1), 156–159 (2011).
18. Z. Xu, Q. Sun, B. Li, Y. Luo, W. Lu, D. Liu, P. P. Shum, and L. Zhang, "Highly sensitive refractive index sensor based on cascaded microfiber knots with Vernier effect," Opt. Express **23**(5), 6662–6672 (2015).
19. H. Liao, P. Lu, X. Fu, X. Jiang, W. Ni, D. Liu, and J. Zhang, "Sensitivity amplification of fiber-optic in-line Mach–Zehnder Interferometer sensors with modified Vernier-effect," Opt. Express **25**(22), 26898–26909 (2017).
20. M. La Notte and V. M. Passaro, "Ultra high sensitivity chemical photonic sensing by Mach–Zehnder interferometer enhanced Vernier-effect," Sens. Actuators, B **176**, 994–1007 (2013).
21. C. Zhu, R. E. Gerald II, and J. Huang, "Ultra-Sensitive Microwave-Photonic Optical Fiber Interferometry Based on Phase-Shift Amplification," IEEE J. Sel. Top. Quantum Electron. **27**(6), 1–8 (2021).
22. C. Zhu and J. Huang, "Microwave-photonic optical fiber interferometers for refractive index sensing with high sensitivity and a tunable dynamic range," Opt. Lett. **46**(9), 2180–2183 (2021).
23. Z. Xu, X. Shu, and H. Fu, "Sensitivity enhanced fiber sensor based on a fiber ring microwave photonic filter with the Vernier effect," Opt. Express **25**(18), 21559–21566 (2017).